RSC Advances

PAPER

View Article Online
View Journal | View Issue

Cite this: *RSC Adv.*, 2024, **14**, 10574

Understanding the decomposition process of the $Pt_1Ag_{24}(SPhCl_2)_{18}$ nanocluster at the atomic level†

Kefan Jiang,[a] Along Ma,[ab] Yuansheng Li,[a] Jiawei Wang,[a] Zhengmao Yin*[a] and Shuxin Wang *[ab]

Received 19th February 2024
Accepted 22nd March 2024

DOI: 10.1039/d4ra01274g

rsc.li/rsc-advances

We report the decomposition of the $Pt_1Ag_{24}(SPhCl_2)_{18}$ nanocluster into a crown-like $Pt_1Ag_4(SR)_8$ (SR = 2,4-$SPhCl_2$ and 4-SPhBr) complex. UV-vis spectra and single crystal X-ray diffraction were used to track the structure-conversion process. Based on the total structure, the differences in ligand exchange rates at different sites and the effects on the stability were mapped out. This work can not only help us understand the ligand exchange behavior of the clusters, but also provide experimental support for the design of stable metal clusters.

1 Introduction

Atomically precise metal nanoclusters can help elucidate the precise relationship between structure and properties,[1–15] which is crucial to comprehend the nanocluster stability,[16–19] transformation mechanism and growth mechanism in solution.[20–25] The interaction between clusters not only can help us understand the interaction of nanoparticles at the atomic level,[26,27] but also aids in designing and synthesizing clusters of specific sizes or characteristics.[28–32] Indeed, based on the ligand-exchange-induced size/structure transformation (LEIST) method, a series of clusters with monodispersity have been synthesized and their structures determined by Single crystal X-ray diffraction (SC-XRD).[33–40] It is worth noting that there are two major behaviours in LEIST: (i) conversion. For instance, the size transformation of the $Au_{38}(SC_2H_4Ph)_{24}$ nanocluster to the $Au_{36}(SPh^tBu)_{24}$ nanocluster induced by $HSPh^tBu$ ligands.[33] More importantly, due to the precise structure, the mechanism of such a process can be studied at the atomic level; (ii) decomposition. In the LESIT method, partial or complete decomposition usually occurs.[22,41,42] For example, the synthesis of the monodisperse $Pt_1Au_{24}(SC_2H_4Ph)_{18}$ nanocluster is accompanied by the decomposition of the $Au_{25}(SC_2H_4Ph)_{18}$ nanocluster.[41] In past research, the process and mechanism of cluster size transformation in LESIT have been extensively studied.[33,43–46] However, understanding the decomposition process of nanoclusters at the atomic level is crucial for us to understand the origin of stability, but there are few studies.

Herein, we monitored the decomposition of $Pt_1Ag_{24}(SPhCl_2)_{18}$ nanoclusters with UV-vis spectra and SC-XRD.[47] We obtained three crystals, including two intermediates ($Pt_1Ag_{24}(SPhCl_2)_{7.51}(SPh^tBr)_{12.49}$, denoted as **NC-I**; $Pt_1Ag_{24}(SPhCl_2)_{2.28}(SPh^tBr)_{17.72}$, denoted as **NC-II**) and one decomposed product ($Pt_1Ag_4(SPhCl_2)_{4.31}(SPh^tBr)_{3.69}$, denoted as Pt_1Ag_4).[45] Through the structural analysis of these crystals and calculating the occupancy ratio of exchanged ligands, the ligand exchange rate at different positions on the clusters has been mapped out.[48] It is worth noting that, although some ligands are located at symmetrical positions on the C_3 axis, the ligand exchange rates show significant differences. These subtle differences lead to the decomposition of the cluster.

2 Experimental methods

2.1 Chemicals

All reagents were purchased from XiLong Scientific and used directly without further purification. Silver nitrate ($AgNO_3$, 99%, metal basis), potassium tetrachloroplatinate (II) (K_2PtCl_4; 99%, metal basis), 2,4-dichlorobenzenethiol ($HSPh^{2,4}Cl_2$, 99%), 4-bromothiophenol ($HSPh^tBr$, 99%), tetraphenylphosphonium bromide (PPh_4Br, 98%), sodium borohydride ($NaBH_4$, 98%), triethylamine ($C_6H_{15}N$, 99.5%), dichloromethane (CH_2Cl_2, HPLC), methanol (CH_3OH, HPLC), *N*,*N*-dimethylformamide (DMF, HPLC), hexane (C_6H_{14}, HPLC), and diethyl ether ($(CH_3CH_2)_2O$, HPLC) were used.

2.2 Synthesis of $Pt_1Ag_{24}(SPhCl_2)_{18}$ nanocluster

The sample of $Pt_1Ag_{24}(SPhCl_2)_{18}$ was synthesized based on the previously reported process with minor modifications.[47]

[a]*College of Materials Science and Engineering, Qingdao University of Science and Technology, Qingdao 266042, P. R. China. E-mail: shuxin_wang@qust.edu.cn; yzm198752@163.com*

[b]*Key Laboratory of Optic-Electric Sensing and Analytical Chemistry for Life Science, MOE, Shandong Key Laboratory of Biochemical Analysis, College of Chemistry and Molecular Engineering, Qingdao University of Science and Technology, Qingdao 266042, China*

† Electronic supplementary information (ESI) available: Details of the experiment, characterization and supporting figures. CCDC 2327471–2327473. For ESI and crystallographic data in CIF or other electronic format see DOI: https://doi.org/10.1039/d4ra01274g

Firstly, $AgNO_3$ (10 mg, 0.0588 mmol) was dissolved in CH_3OH. CH_2Cl_2 and K_2PtCl_4 (10 mg, 0.0240 mmol) were then added to the solution to form a pale-yellow mixture. In an ice bath, the mixture was cooled to 0 °C. Then, 2,4-dichlorobenzenethiol (10 μL, 0.0791 mmol) and tetraphenylphosphonium bromide (10 mg, 0.0238 mmol) were added in turn. After 30 min, 1 mL $NaBH_4$ aqueous solution (40 mg mL^{-1}, 1.057 mmol) and triethylamine (50 μL, 0.358 mmol) were added quickly to the mixture under vigorous stirring. This reaction was further aged for 12 h at 0 °C. Whereafter, the aqueous phase was removed. The mixture in the organic phase was washed three times with $(CH_3CH_2)_2O$ (2 × 10 mL). After a week, dark-red crystals were acquired in CH_2Cl_2/hexane at room temperature.

2.3 Conversion from $Pt_1Ag_{24}(SPhCl_2)_{18}$ to $Pt_1Ag_4(SR)_8$

Briefly, $Pt_1Ag_{24}(SPhCl_2)_{18}$ (10 mg, 0.00167 mmol) crystals were dissolved in 5 mL DMF, then HSPh^{t}Br was added in different molar ratios. The progress of the reaction is less dependent on the time, and is highly dependent on the molar ratio of HSPh^{t}Br mercaptan ligand added. After the addition of 200 equivalents of HSPh^{t}Br, all $Pt_1Ag_{24}(SPhCl_2)_{18}$ nanoclusters were converted to $Pt_1Ag_4(SR)_8$ complexes. The crude products of $Pt_1Ag_4(SR)_8$ were washed two times with $(CH_3CH_2)_2O$ (2 × 10 mL). Single crystal growth of $Pt_1Ag_{24}(SR)_{20}$ and $Pt_1Ag_4(SR)_8$ was accomplished by vapor diffusion of $(CH_3CH_2)_2O$ into a concentrated solution of the $Pt_1Ag_4(SR)_8$ in CH_2Cl_2 for 2 days.

2.4 Synthesis of NC-I and NC-II

In the process of transforming $Pt_1Ag_{24}(SPhCl_2)_{18}$ to $Pt_1Ag_4(SR)_8$, the reaction was halted at a distinctive juncture. For **NC-I**, after 60 equivalents of HSPh^{t}Br was added and followed by stirring 3 minutes, the reaction was terminated. For **NC-II**, after 100 equivalents of HSPh^{t}Br was added and followed by stirring for 3 minutes, the reaction was terminated. The crude products of **NC-I** and **NC-II** were washed two times with $(CH_3CH_2)_2O$ (2 × 10 mL). Single crystal growth of **NC-I** and **NC-II** was accomplished through vapor diffusion of $(CH_3CH_2)_2O$ into a concentrated solution of the **NC-I** and **NC-II** in CH_2Cl_2 for 2 days.

2.5 Characterization

All UV-vis absorption spectra of the structure conversion process were acquired on UV-1810 at room temperature. The data collections for single crystal X-ray diffraction were carried out on a STOE stadivari diffractometer. Data reductions and absorption corrections were performed using the X-Area. The structure was solved by intrinsic phasing and refined with full-matrix least squares on F^2 using the SHELXTL software package. All non-hydrogen atoms were refined anisotropically, and all the hydrogen atoms were set in geometrically calculated positions and refined isotopically using a riding model. In order to confirm the ligand type of the cluster, the Br position was refined as free variables.

3 Results and discussion

3.1 Monitoring the transformation process from $Pt_1Ag_{24}(SPhCl_2)_{18}$ to $Pt_1Ag_4(SR)_8$

In this work, our focus centered on the decomposition of metal nanoclusters, and we selected $Pt_1Ag_{24}(SPhCl_2)_{18}$ (where, $SPhCl_2$ = 2,4-dichlorothiolated) nanocluster as the model due to its metastability in the presence of aryl mercaptan.[45,49–51] As shown in Fig. 1, the UV-vis absorption spectrum of $Pt_1Ag_{24}(SPhCl_2)_{18}$ nanocluster exhibits two characteristic absorption peaks at 455 nm and 570 nm, with a shoulder at 400 nm, consistent with the reported result.[47] $Pt_1Ag_{24}(SPhCl_2)_{18}$ nanocluster was converted into $Pt_1Ag_{24}(SR)_{20}$ (where SR is the mixture of 2,4-$SPhCl_2$ and 4-SPhBr) nanocluster after adding less than 60 equivalents of 4-bromothiophenol ligand (HSPh^{t}Br), which is similar to the reported results.[45] Where characteristic absorptions of $Pt_1Ag_{24}(SR)_{20}$ (at 400 nm, 435 nm, 480 nm, and 575 nm) became prominent, while those of $Pt_1Ag_{24}(SPhCl_2)_{18}$ (455 nm, 570 nm and 400 nm) diminished. In this series of spectra, four isosbestic points were discovered at 400, 420, 480, and 505 nm, signifying the process is quantitative. Simultaneously, the colour of the solution turned from atrovirens to reddish orange (Fig. S1†). The reason for the transformation from $Pt_1Ag_{24}(SPhCl_2)_{18}$ to $Pt_1Ag_{24}(SR)_{20}$ is that three $Ag_2(SR)_3$ staple motifs of $Pt_1Ag_{24}(SPhCl_2)_{18}$ are aggregated to be one $Ag_6(SR)_{10}$ surface caps at nanocluster poles by the addition and induction of free thiol ligands. After adding 60 equivalents of 4-bromothiophenol ligand, the absorbance of the sample decreases as the amount of ligand increases. The constant peak position and the ratio of the different peaks indicate the clusters have been gradually decomposed into complexes. After adding 200 equivalents of HSPh^{t}Br to the solution, there is no peak after 400 nm, indicating that the nanoclusters are completely decomposed into metal complexes. Concurrently, the colour of the solution turned from reddish orange to pale yellow (Fig. S1†).

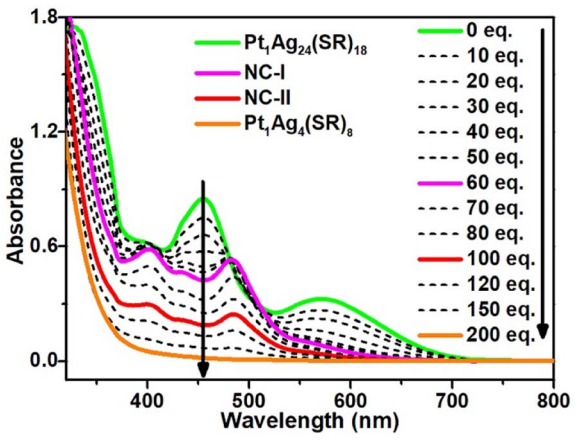

Fig. 1 The UV-vis absorption spectra of transformation process from $Pt_1Ag_{24}(SPhCl_2)_{18}$ nanocluster to $Pt_1Ag_4(SR)_8$ complex. The UV-vis absorption spectra with diverse ratios of HSPh^{t}Br mercaptan ligand to $Pt_1Ag_{24}(SPhCl_2)_{18}$ nanocluster; (eq. represents the molar ratio of HSPh^{t}Br mercaptan to $Pt_1Ag_{24}(SPhCl_2)_{18}$ nanocluster).

3.2 Crystal structure of $Pt_1Ag_{24}(SR)_{20}$ and $Pt_1Ag_4(SR)_8$

To elucidate the detailed decomposition process of this nanocluster, the reaction was stopped at the specific molar ratios.[52] As shown in Fig. 1 (solid line), the crystal of **$Pt_1Ag_{24}(SPhCl_2)_{7.51}(SPh^tBr)_{12.49}$** (magenta line, **NC-I**), **$Pt_1Ag_{24}(SPhCl_2)_{2.28}(SPh^tBr)_{17.72}$** (red line, **NC-II**) and **$Pt_1Ag_4(SPhCl_2)_{4.31}(SPh^tBr)_{3.69}$** (orange line, **$Pt_1Ag_4(SR)_8$**) were obtained (Fig. S2†). SC-XRD was used to determine the overall structure of these crystals, respectively (Fig. S3†). Additionally, UV-vis spectra of **NC-I**, **NC-II**, and **Pt_1Ag_4** crystals are shown in Fig. S4 and S5.† Results revealed that **NC-I** exhibits two strong absorption peaks at 400 nm and 482 nm, with two weaker peaks at 435 nm and 575 nm (Fig. S4†). Similarly, **NC-II** also showed two main absorption peaks (397 nm and 480 nm) and two weaker peaks (432 nm and 564 nm). Compared to **NC-I**, a blue shift was observed in the UV-vis spectrum of **NC-II**, attributed to different occupancy ratios of ligands. **Pt_1Ag_4** composite only displayed a faint peak at 442 nm (Fig. S5†).

The crystal structure analysis of **$Pt_1Ag_{24}(SR)_{20}$** and **$Pt_1Ag_4(SR)_8$** is presented in Fig. 2. For the **$Pt_1Ag_{24}(SR)_{20}$** nanocluster, the entire **$Pt_1Ag_{24}(SR)_{20}$** structure exhibits an icosahedral Pt_1Ag_{12} metal kernel protected by two $Ag_6(SR)_{10}$ staple motifs (Fig. 2a–c).[45] Consequently, the overall framework of **$Pt_1Ag_{24}(SR)_{20}$** can be regarded as "Pt_1Ag_{12} + 2*$Ag_6(SR)_{10}$". Each $Ag_6(SR)_{10}$ motif comprises three irregular hexagons (Fig. 2a), where three irregular hexagons are fused together by sharing the Ag–SR–Ag edges and terminated with three SR ligands. In the **$Pt_1Ag_4(SR)_8$** complex (Fig. 2d–f), the Pt atom exists independently of the Ag_4 plane, with an average distance of 3.4 Å. Among the eight bridging thiolates, four bridging thiolates are bonded to Pt and Ag atoms, while the others link between two Ag atoms. Alternatively, the structure of **$Pt_1Ag_4(SR)_8$** can be viewed as two layers: the upper layer (A layer) resembles "a cross" with $Pt_1(SR)_4$, and the lower layer (B layer) is $Ag_4(SR)_4$, akin to "a plate". Notably, the entire structure of **$Pt_1Ag_4(SR)_8$** exhibits C_4 Axial Symmetry (Fig. 2d). The Ag–Ag bonds in the **Pt_1Ag_4** kernel range from 3.067 to 3.165 Å (average: 3.115 Å), surpassing the Ag–Ag bond distance (2.889 Å) in bulk silver. Additionally, the Pt–S bonds range from 2.327 to 2.334 Å (average: 2.331 Å). There are two kinds of bridging thiolates in **$Pt_1Ag_4(SR)_8$** complex,[53] with average Pt–S–Ag angle of 87.64 to 89.03° (average: 88.33°) and Ag–S–Ag angle of 77.22 to 79.63° (average: 78.26°). The clockwise and anticlockwise of the thiol ligands reveal the **$Pt_1Ag_4(SR)_8$** complex is racemic (Fig. 2f and S6†).[25]

Building upon the aforementioned results, the transformation from **$Pt_1Ag_{24}(SPhCl_2)_{18}$** to **$Pt_1Ag_4(SR)_8$** can be classified into two stages. A comprehensive diagram of the entire transformation process is depicted in Fig. 3. According to the symmetry of the crystal, only half of the $Ag_2(SR)_3$ motif for **$Pt_1Ag_{24}(SR)_{18}$** and the $Ag_6(SR)_{10}$ motif for **$Pt_1Ag_{24}(SR)_{20}$** are shown in Fig. 3 for clarity. To better illustrate the variation in ligand occupancy ratio and species during the conversion process, S atoms were used as substitutes for the entire mercaptan ligands. And all ligands were divided into three categories: ligands completely occupied by 2,4-$SPhCl_2$ were highlighted in yellow, ligands absolutely occupied by 4-SPhBr were represented by red atoms and ligands occupied by both 2,4-$SPhCl_2$ and 4-SPhBr were highlighted in turquois.

Stage 1: In the first stage (from 0 eq. to 60 eq.), **$Pt_1Ag_{24}(SPhCl_2)_{18}$** was converted to **$Pt_1Ag_{24}(SPhCl_2)_{7.51}(SPh^tBr)_{12.49}$** (**NC-I**), matching the UV-vis spectra from 0 eq. to 60 eq. (Fig. 1) and the transformation process from **$Pt_1Ag_{24}(SPhCl_2)_{18}$** (Fig. 3a) to **NC-I** (Fig. 3b). The average number of 2,4-$SPhCl_2$ reached *ca.* 7.51 in **NC-I**. Stage 2: In the second stage (from 60 eq. to 200 eq.), as shown in Fig. 3b–e, **$Pt_1Ag_{24}(SPhCl_2)_{7.51}(SPh^tBr)_{12.49}$** (**NC-I**) was decomposed into **$Pt_1Ag_4(SR)_8$** or exchanged by the $HSPh^tBr$ ligand into **$Pt_1Ag_{24}(SPhCl_2)_{2.28}(SPh^tBr)_{17.72}$** (**NC-II**) with the addition of $HSPh^tBr$ mercaptan. The average number of 2,4-$SPhCl_2$ in **NC-II** reached a maximum of approximately 2.28. Further, **NC-II** was also decomposed into **$Pt_1Ag_4(SR)_8$**. Detailed crystal parameters were provided in Tables S1–S3.† Additionally, the disparate occupancy ratios of ligands within **NC-I** and **NC-II** nanoclusters result in their respective crystallization in

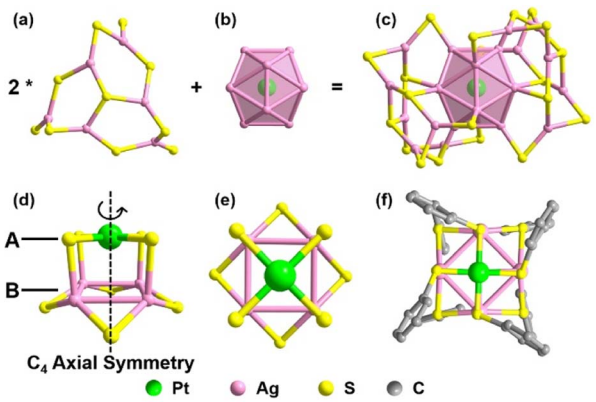

Fig. 2 Structural anatomy of $Pt_1Ag_{24}(SR)_{20}$ and $Pt_1Ag_4(SR)_8$. (a) Two $Ag_6(SR)_{10}$ staple motifs of $Pt_1Ag_{24}(SR)_{20}$; (b) the Pt_1Ag_{12} kernel of $Pt_1Ag_{24}(SR)_{20}$; (c) X-ray structure of the $Pt_1Ag_{24}(SR)_{20}$; (d) X-ray structure of the $Pt_1Ag_4(SR)_8$; (e) top view of the $Pt_1Ag_4(SR)_8$ framework; (f) top view of the overall structure of $Pt_1Ag_4(SR)_8$. Color labels: bright green = Pt; pink = Ag; yellow = S; grey = C. H, Cl, Br atoms and some carbon atoms are omitted for clarity.

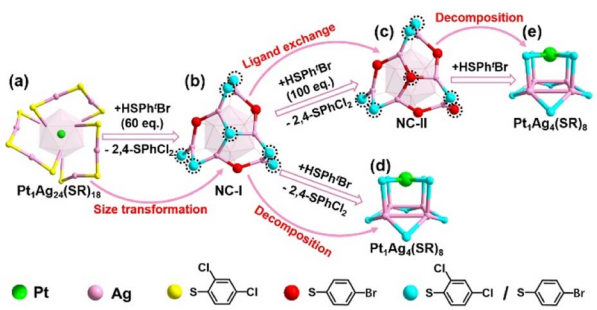

Fig. 3 Transformation pathway from $Pt_1Ag_{24}(SR)_{18}$ to $Pt_1Ag_4(SR)_8$. (a) Partial structure of the $Pt_1Ag_{24}(SPhCl_2)_{18}$: Pt_1Ag_{12} core + 3*$Ag_2(SR)_3$ motifs; (b) partial structure of the **NC-I**: Pt_1Ag_{12} core + $Ag_6(SR)_{10}$ top unit; (c) partial structure of the **NC-II**: Pt_1Ag_{12} core + $Ag_6(SR)_{10}$ top unit; (d) and (e) overall structure of the $Pt_1Ag_4(SR)_8$. Color labels: bright green = Pt; pink = Ag; yellow = 2,4-$SPhCl_2$; red = 4-SPhBr; turquois = 2,4-$SPhCl_2$/4-SPhBr; H, C, Cl and Br atoms are omitted for clarity.

distinct crystal systems—triclinic and monoclinic systems (Fig. S7†). Furthermore, this further impacts the arrangement of cluster molecules, as although the cluster molecules of **NC-I** and **NC-II** are arranged in an "ABAB" pattern, the orientation of the molecules' arrangement is entirely different (Fig. S8†).[15,54]

3.3 The conversion mechanism from $Pt_1Ag_{24}(SR)_{18}$ to $Pt_1Ag_4(SR)_8$

As illustrated in Fig. 3, both **NC-I** and **NC-II** nanoclusters show similar structures. The variance in the occupancy ratio of 2,4-$SPhCl_2$ and 4-SPhBr ligands reveals the ligand exchange process of nanoclusters (Table S4†). Notably, **NC-I** and **NC-II**, along with Pt_1Ag_4, were examined for the occupancy ratios (x%) of 2,4-$SPhCl_2$ in mercaptan ligands, as depicted in Fig. 4.[45,55,56] To enhance clarity, we categorized ten mercaptan ligands into four types in **NC-I** and **NC-II**: type I (ligand-1, ligand-2, and ligand-3), type II (ligand-4, ligand-5, and ligand-6), type III (ligand-7, ligand-8, and ligand-9), and type IV (ligand-10).

The occupancy ratios of 2,4-$SPhCl_2$ and 4-SPhBr units in **NC-I**, **NC-II**, and Pt_1Ag_4 were summarized in Table S4,† and detailed information about related bonds is shown in Table S5.† Obviously, the exchange sites of type III (ligand-7, ligand-8 and ligand-9) were completely exchanged by 4-SPhBr ligands in **NC-I** (Fig. 4a), indicating that thiol ligands in type III are more susceptible to be exchanged. Similarly, the occupancy ratio of 2,4-$SPhCl_2$ to type IV (ligand-10) is only 10% in **NC-I** (Fig. 4a), and is fully exchanged by 4-SPhBr in **NC-II** (Fig. 4b). The occupancy ratios of 2,4-$SPhCl_2$ at these four ligand sites in **NC-I** and **NC-II** suggest that they are not critical for the decomposition of the $Pt_1Ag_{24}(SR)_{20}$ nanocluster. For the ligands of type I, the occupancy ratio of 2,4-$SPhCl_2$ to ligand-1 in **NC-I** was 50%, decreasing to 14% in **NC-II**. Concurrently, the ratio of ligand-2 and ligand-3 also decreased. Fig. 4 and Table S4† showed the following ratio of ligand-2: **NC-I**/**NC-II** = 42%/24%, and ligand-3: **NC-I**/**NC-II** = 79%/25%. Regarding the ligands of type II, at these positions, the occupancy ratios of 2,4-$SPhCl_2$ in these three ligands significantly decrease from **NC-I** to **NC-II** (Fig. 4a, b and Table S4†). Specifically, in **NC-I** and **NC-II**, the occupancy ratios of 2,4-$SPhCl_2$ in ligand-4 are 71.6% and 0% (Fig. 4a, b and Table S4†), respectively, indicating that 2,4-$SPhCl_2$ units were fully exchanged by 4-SPhBr in **NC-II**. Fig. 4 and Table S4† showed the following occupancy ratios of 2,4-$SPhCl_2$ in the ligands of type II, ligand-5: **NC-I**/**NC-II** = 60.7%/22% and ligand-6: **NC-I**/**NC-II** = 62.3%/29%, respectively. However, the relevant S–Ag bond lengths in **NC-I** and **NC-II** did not change significantly (Table S5†).

According to the analysis of the occupancy ratios of 2,4-$SPhCl_2$ in the ten ligands, we found that four ligands of type III and type IV were independent of the decomposition of $Pt_1Ag_{24}(SR)_{20}$. Additionally, due to the significantly higher occupancy ratios of 2,4-$SPhCl_2$ in Pt_1Ag_4 compared to **NC-II** (Fig. 4b, c and Table S4†), and considering the abundant presence of $HSPh^tBr$ thiol ligands in the solution, it is impossible that the 2,4-$SPhCl_2$ and 4-SPhBr units in Pt_1Ag_4 to originate from **NC-II**. Furthermore, for the six mercaptan ligands of type I and type II, the average occupancy ratio of the 2,4-$SPhCl_2$ unit in NC-I (average: 0.609) is similar to the average occupancy ratio of 2,4-$SPhCl_2$ in $Pt_1Ag_4(SR)_8$ (average: 0.539) in Fig. 4a, c and Table S4.† Based on existing technology, it is difficult to directly observe the transfer process of a single ligand/metal in the nanocluster transformation process. It is reasonable to assume that the most likely reason for the similar ratio is that the ligands on the $Pt_1Ag_4(SR)_8$ complex are inherited from the ligands of type I and type II in **NC-I**. We proposed the possible decomposition mechanism of the $Pt_1Ag_{24}(SR)_{18}$ nanocluster (Fig. 5). One Pt atom, four Ag atoms and eight mercaptan ligands containing 2,4-$SPhCl_2$ and 4-SPhBr units formed $Pt_1Ag_4(SR)_8$. And one central Pt atom, twelve thiol ligands of type I and type II, and sixteen Ag atoms connected to twelve thiol ligands in **NC-I** are potential sources of one Pt atom, eight thiol ligands and four silver atoms in Pt_1Ag_4.

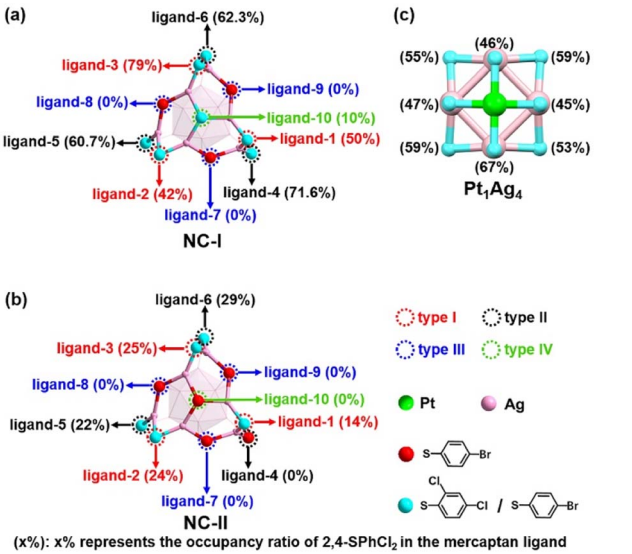

Fig. 4 The corresponding occupancy ratios of 2,4-$SPhCl_2$ unit in **NC-I**, **NC-II** and Pt_1Ag_4. (a) Partial structure of the **NC-I** (Pt_1Ag_{12} kernel + $Ag_6(SR)_{10}$ top unit) was displayed to explain the type of ligand. (b) Partial structure of the **NC-II** (Pt_1Ag_{12} core + $Ag_6(SR)_{10}$ top unit) was displayed to explain the type of ligand. (c) The structure of the Pt_1Ag_4 was displayed. The occupancy ratios of 2,4-$SPhCl_2$ unit were displayed in (x%). Color labels: bright green = Pt; pink = Ag; red = 4-SPhBr; turquois = 2,4-$SPhCl_2$ and 4-SPhBr. H, C, Cl and Br atoms are omitted for clarity. Notably, the occupancy ratios of **NC-I** are the average occupancy ratios among the three cluster molecules in single crystal.

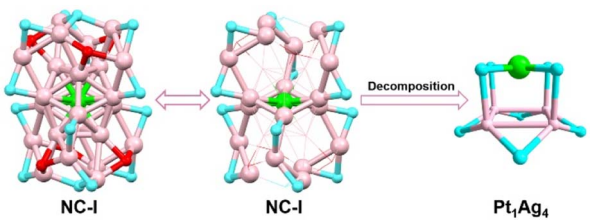

Fig. 5 The possible decomposition mechanism from **NC-I** nanocluster to $Pt_1Ag_4(SR)_8$ complex. Color labels: bright green = Pt; pink = Ag; red = 4-SPhBr; turquois = 2,4-$SPhCl_2$ and 4-SPhBr. H, C, Cl and Br atoms are omitted for clarity.

4 Conclusions

In summary, we have presented a study on the decomposition of $Pt_1Ag_{24}(SPhCl_2)_{18}$ nanocluster leading to the formation of the $Pt_1Ag_4(SR)_8$ complex. This process was monitored using UV-vis spectra and SC-XRD. The pathway of transformation can be roughly divided into two stages: (I) HSPh^{t}Br-triggered size transformation of $Pt_1Ag_{24}(SPhCl_2)_{18}$ forms **NC-I**; (II) structural decomposition of **NC-I** to $Pt_1Ag_4(SR)_8$ and ligand exchange of **NC-I** to **NC-II**. And $Pt_1Ag_4(SR)_8$ complex is inherited from the Pt atom, partial Ag atoms, and the ligand containing 2,4-SPhCl$_2$ and 4-SPhBr in **NC-I**.

Conflicts of interest

There are no conflicts to declare.

Acknowledgements

We acknowledge the financial support provided by the National Natural Science Foundation of China (21803001 and 21771156) and Start-up Funding from Qingdao University of Science and Technology.

Notes and references

1 B. Bhattarai, Y. Zaker, A. Atnagulov, B. Yoon, U. Landman and T. P. Bigioni, *Acc. Chem. Res.*, 2018, **51**, 3104–3113.
2 A. W. Cook and T. W. Hayton, *Acc. Chem. Res.*, 2018, **51**, 2456–2464.
3 K. Konishi, M. Iwasaki and Y. Shichibu, *Acc. Chem. Res.*, 2018, **51**, 3125–3133.
4 Z. Lei, X. K. Wan, S. F. Yuan, Z. J. Guan and Q. M. Wang, *Acc. Chem. Res.*, 2018, **51**, 2465–2474.
5 R. L. Whetten, H. C. Weissker, J. J. Pelayo, S. M. Mullins, X. Lopez-Lozano and I. L. Garzon, *Acc. Chem. Res.*, 2019, **52**, 34–43.
6 Q. F. Yao, T. K. Chen, X. Yuan and J. P. Xie, *Acc. Chem. Res.*, 2018, **51**, 1338–1348.
7 Q.-F. Zhang, X. Chen and L.-S. Wang, *Acc. Chem. Res.*, 2018, **51**, 2159–2168.
8 Y. Z. Lu and W. Chen, *Chem. Soc. Rev.*, 2012, **41**, 3594–3623.
9 S. Wang, S. Jin, S. Yang, S. Chen, Y. Song, J. Zhang and M. Zhu, *Sci. Adv.*, 2015, **1**, e1500441.
10 L. Tang, Y. Luo, X. Ma, B. Wang, M. Ding, R. Wang, P. Wang, Y. Pei and S. Wang, *Angew. Chem., Int. Ed.*, 2023, **62**, e202300553.
11 L. Tang, A. Ma, C. Zhang, X. Liu, R. Jin and S. Wang, *Angew. Chem., Int. Ed.*, 2021, **60**, 17969–17973.
12 Y. Yun, H. Sheng, K. Bao, L. Xu, Y. Zhang, D. Astruc and M. Zhu, *J. Am. Chem. Soc.*, 2020, **142**, 4126–4130.
13 S. Wang, X. Meng, A. Das, T. Li, Y. Song, T. Cao, X. Zhu, M. Zhu and R. Jin, *Angew. Chem., Int. Ed.*, 2014, **53**, 2376–2380.
14 X. Wang, B. Yin, L. Jiang, C. Yang, Y. Liu, G. Zou, S. Chen and M. Zhu, *Science*, 2023, **381**, 784–790.
15 A. Ma, J. Wang, Y. Wang, Y. Zuo, Y. Ren, X. Ma and S. Wang, *Polyoxometalates*, 2024, **3**, 9140054.
16 H. Shen, L. Wang, O. López-Estrada, C. Hu, Q. Wu, D. Cao, S. Malola, B. K. Teo, H. Häkkinen and N. Zheng, *Nano Res.*, 2021, **14**, 3303–3308.
17 Y. Li, H. K. Kim, R. D. McGillicuddy, S.-L. Zheng, K. J. Anderton, G. J. Stec, J. Lee, D. Cui and J. A. Mason, *J. Am. Chem. Soc.*, 2023, **145**, 9304–9312.
18 S. K. Barik, T.-H. Chiu, Y.-C. Liu, M.-H. Chiang, F. Gam, I. Chantrenne, S. Kahlal, J.-Y. Saillard and C. W. Liu, *Nanoscale*, 2019, **11**, 14581–14586.
19 H. Chen, L. Peng, Y. Bian, X. Shen, J. Li, H.-C. Yao, S.-Q. Zang and Z. Li, *Appl. Catal., B*, 2021, **284**, 119704.
20 L. Tang, X. Kang, X. Wang, X. Zhang, X. Yuan and S. Wang, *Inorg. Chem.*, 2021, **60**, 3037–3045.
21 R. Itteboina, U. D. Madhuri, P. Ghosal, M. Kannan, T. K. Sau, T. Tsukuda and S. Bhardwaj, *J. Phys. Chem. A*, 2018, **122**, 1228–1234.
22 Y. Negishi, H. Horihata, A. Ebina, S. Miyajima, M. Nakamoto, A. Ikeda, T. Kawawaki and S. Hossain, *Chem. Sci.*, 2022, **13**, 5546–5556.
23 Y. Tan, Y. Lv, L. Xu, Q. Li, J. Chai, S. Yang, H. Yu and M. Zhu, *J. Am. Chem. Soc.*, 2023, **145**, 4238–4245.
24 S. Chen, S. Wang, J. Zhong, Y. Song, J. Zhang, H. Sheng, Y. Pei and M. Zhu, *Angew. Chem., Int. Ed.*, 2015, **54**, 3145–3149.
25 A. Ma, W. Du, J. Wang, K. Jiang, C. Zhang, W. Sheng, H. Zheng, R. Jin and S. Wang, *J. Phys. Chem. Lett.*, 2023, **14**, 5095–5101.
26 K. R. Krishnadas, A. Ghosh, A. Baksi, I. Chakraborty, G. Natarajan and T. Pradeep, *J. Am. Chem. Soc.*, 2016, **138**, 140–148.
27 K. R. Krishnadas, A. Baksi, A. Ghosh, G. Natarajan and T. Pradeep, *Nat. Commun.*, 2016, **7**, 13447.
28 L. Xu, Q. Li, T. Li, J. Chai, S. Yang and M. Zhu, *Inorg. Chem. Front.*, 2021, **8**, 4820–4827.
29 Y.-D. Cao, D. Yin, S. Li, X.-Y. Dong, Y. Feng, H. Liu, L.-L. Fan, G.-G. Gao and S.-Q. Zang, *Angew. Chem., Int. Ed.*, 2023, **62**, e202307678.
30 H. Shan, J. Shi, T. Chen, Y. Cao, Q. Yao, H. An, Z. Yang, Z. Wu, Z. Jiang and J. Xie, *ACS Nano*, 2023, **17**, 2368–2377.
31 X. Wei, X. Kang, Z. Zuo, F. Song, S. Wang and M. Zhu, *Natl. Sci. Rev.*, 2020, **8**, nwaa077.
32 S. Chen, W. Du, C. Qin, D. Liu, L. Tang, Y. Liu, S. Wang and M. Zhu, *Angew. Chem., Int. Ed.*, 2020, **59**, 7542–7547.
33 C. J. Zeng, C. Y. Liu, Y. Pei and R. C. Jin, *ACS Nano*, 2013, **7**, 6138–6145.
34 M. S. Bootharaju, C. P. Joshi, M. J. Alhilaly and O. M. Bakr, *Chem. Mater.*, 2016, **28**, 3292–3297.
35 H. W. Dong, L. W. Liao and Z. K. Wu, *J. Phys. Chem. C*, 2017, **8**, 5338–5343.
36 A. Baghdasaryan, E. Brun, Y. Wang, G. Salassa, J. Lacour and T. Buergi, *Chem. Sci.*, 2021, **12**, 7419–7427.
37 C. L. Heinecke, T. W. Ni, S. Malola, V. Makinen, O. A. Wong, H. Hakkinen and C. J. Ackerson, *J. Am. Chem. Soc.*, 2012, **134**, 13316–13322.

38 Z. H. Tang, T. Ahuja, S. M. Wang and G. L. Wang, *Nanoscale*, 2012, **4**, 4119–4124.
39 W. Du, S. Jin, L. Xiong, M. Chen, J. Zhang, X. Zou, Y. Pei, S. Wang and M. Zhu, *J. Am. Chem. Soc.*, 2017, **139**, 1618–1624.
40 X. Zou, X. Kang and M. Zhu, *Chem. Soc. Rev.*, 2023, **52**, 5892–5967.
41 H. F. Qian, D. E. Jiang, G. Li, C. Gayathri, A. Das, R. R. Gil and R. C. Jin, *J. Am. Chem. Soc.*, 2012, **134**, 16159–16162.
42 Y. Niihori, W. Kurashige, M. Matsuzaki and Y. Negishi, *Nanoscale*, 2013, **5**, 508–512.
43 T. Dainese, S. Antonello, S. Bogialli, W. W. Fei, A. Venzo and F. Maran, *ACS Nano*, 2018, **12**, 7057–7066.
44 Y. A. Wang, B. Nieto-Ortega and T. Burgi, *Chem. Commun.*, 2019, **55**, 14914–14917.
45 X. W. X. Kang, S. Jin, S. Wang and M. Zhu, *CCS Chem.*, 2021, **3**, 1929–1939.
46 J.-H. Yu, Z.-R. Yuan, J. Xu, J.-G. Wang, M. Azam, T.-D. Li, Y.-Z. Li and D. Sun, *Chem. Sci.*, 2023, **14**, 6564–6571.
47 J. Z. Yan, H. F. Su, H. Y. Yang, S. Malola, S. C. Lin, H. Hakkinen and N. F. Zheng, *J. Am. Chem. Soc.*, 2015, **137**, 11880–11883.
48 K. H. Wijesinghe, N. A. Sakthivel, T. Jones and A. Dass, *J. Phys. Chem. C*, 2020, **11**, 6312–6319.
49 H. Shen, E. Selenius, P. Ruan, X. Li, P. Yuan, O. Lopez-Estrada, S. Malola, S. Lin, B. K. Teo, H. Häkkinen and N. Zheng, *Chem.–Eur. J.*, 2020, **26**, 8465–8470.
50 Q. Z. Li, S. Yang, T. Chen, S. Jin, J. S. Chai, H. Zhang and M. Z. Zhu, *Nanoscale*, 2020, **12**, 23694–23699.
51 C. Zhu, T. Duan, H. Li, X. Wei, X. Kang, Y. Pei and M. Zhu, *Inorg. Chem. Front.*, 2021, **8**, 4407–4414.
52 S. Wang, Y. Tan, T. Li, Q. Zhou, P. Li, S. Yang, H. Yu and M. Zhu, *Inorg. Chem.*, 2022, **61**, 18450–18457.
53 C. Zeng, T. Li, A. Das, N. L. Rosi and R. Jin, *J. Am. Chem. Soc.*, 2013, **135**, 10011–10013.
54 A. Ma, J. Wang, J. Kong, Y. Ren, Y. Wang, X. Ma, M. Zhou and S. Wang, *Phys. Chem. Chem. Phys.*, 2023, **25**, 9772–9778.
55 N. A. Sakthivel, M. Stener, L. Sementa, M. Medves, G. Ramakrishna, A. Fortunelli, A. G. Oliver and A. Dass, *J. Phys. Chem. C*, 2019, **123**, 29484–29494.
56 C. Kumara, C. M. Aikens and A. Dass, *J. Phys. Chem. Lett.*, 2014, **5**, 461–466.